Global and Planetary Change 146 (2016) 179–189

Contents lists available at ScienceDirect

Global and Planetary Change

journal homepage: www.elsevier.com/locate/gloplacha

Invited research article

A probabilistic approach to 21st century regional sea-level projections using RCP and High-end scenarios

Luke P. Jackson [a,b,*], Svetlana Jevrejeva [a]

[a] National Oceanography Centre, 6 Brownlow Street, Liverpool, L3 5DA, UK
[b] Programme for Economic Modelling, Nuffield College, 1 New Road, Oxford University, OX1 1NF, UK

ARTICLE INFO

Article history:
Received 24 February 2016
Received in revised form 3 October 2016
Accepted 5 October 2016
Available online 6 October 2016

Keywords:
Sea-level projection
Probability
Uncertainty
RCP scenarios
Climate change

ABSTRACT

Sea-level change is an integrated climate system response due to changes in radiative forcing, anthropogenic land-water use and land-motion. Projecting sea-level at a global and regional scale requires a subset of projections - one for each sea-level component given a particular climate-change scenario. We construct relative sea-level projections through the 21st century for RCP 4.5, RCP 8.5 and High-end (RCP 8.5 with increased ice-sheet contribution) scenarios by aggregating spatial projections of individual sea-level components in a probabilistic manner. Most of the global oceans adhere to the projected global average sea level change within 5 cm throughout the century for all scenarios; however coastal regions experience localised effects due to the non-uniform spatial patterns of individual components. This can result in local projections that are 10's of centimetres different from the global average by 2100. Early in the century, RSL projections are consistent across all scenarios, however from the middle of the century the patterns of RSL for RCP scenarios deviate from the High-end where the contribution from Antarctica dominates. Similarly, the uncertainty in projected sea-level is dominated by an uncertain Antarctic fate. We also explore the effect upon projections of, treating CMIP5 model ensembles as normally distributed when they might not be, correcting CMIP5 model output for internal variability using different polynomials and using different unloading patterns of ice for the Greenland and Antarctic ice sheets.

1. Introduction

Sea-level rise will affect low lying coastal settlements and ecosystems by means of gradual encroachment and short term flooding due to storms (e.g. Rowley et al., 2007; Hallegatte et al., 2013; Kopp et al., 2014). Whilst global mean sea-level (GMSL) change can be approximated by the sum of ocean expansion (steric), land-ice (Glaciers, Greenland and Antarctica) and land-hydrology components, relative sea-level (RSL) change is more complex due to the spatial variability of, local ocean processes, mass-based sea-level components and vertical land-motion (tectonic and environmental).

While published RSL projections are an aggregate of projected sea-level components, differences lie in the methods used to estimate the individual components. Spada et al. (2013) used one (General Circulation Model) GCM to output ocean processes (steric and dynamic sea level) whilst using temperature and precipitation to estimate land-ice contributions to sea level via regional climate models. Perrette et al. (2013) derived scaling relationships between individual sea-level components and global temperature to create scenario independent patterns, which could be multiplied by scenario specific global temperature projections. Slangen et al. (2014a), Kopp et al. (2014) and Grinsted et al. (2015) calculated ocean processes by averaging over multi-model ensembles of thermo-steric sea-level and dynamic sea-level from Coupled Model Inter-comparison Project Phase 5 (CMIP5, Taylor et al., 2012). Added to these ocean processes, Slangen et al. (2014a) estimated mass-changes in land-ice from model-based projections of temperature and precipitation, while Kopp et al. (2014) and Grinsted et al. (2015) multiplied the GMSL projection of land-ice sea-level components by their associated normalised spatial pattern (fingerprint) of sea-level. Land-hydrology may be treated as a global average (e.g. Kopp et al., 2014) or spatially variable term (e.g. Slangen et al., 2014a; Grinsted et al., 2015) whilst vertical land-movement is either omitted (e.g. Spada et al., 2013; Perrette et al., 2013), conservatively estimated using a glacial isostatic adjustment (GIA) model (e.g. Slangen et al., 2014a; Grinsted et al., 2015) or locally refined (e.g. Kopp et al., 2014).

A feature of Kopp et al. (2014) and Grinsted et al. (2015) was their approach to uncertainty in which they accounted for the probability of a given sea-level by sampling the probability distribution function (either Gaussian or skewed) for each component at each time. In this paper, we present RSL projections using a similar approach to Grinsted et al. (2015) and Kopp et al. (2014). We use a greater range of model outputs from CMIP5 to explore the effect of data preparation upon projected ocean processes. We show how probability density

* Corresponding author.
E-mail address: luke.jackson@economics.ox.ac.uk (L.P. Jackson).

http://dx.doi.org/10.1016/j.gloplacha.2016.10.006

functions (PDFs) of individual component's GMSL projections are derived and how these are used in combination with fingerprints for each sea-level component to construct RSL projections. We then present the resulting projections through time for three scenarios, Representative Concentration Pathway (RCP) 4.5, 8.5 (Moss et al., 2010) and High-end (RCP 8.5 with high-magnitude, low-probability ice-sheet contribution) with their associated uncertainties. Next we discuss the differences between our projections and others recently published, in particular differences in uncertainty. Finally we consider the effect upon regionally projected uncertainty using alternative spatial fields for certain sea-level components.

2. Data and methods

The method used to approximate RSL is the same as that for GMSL with the incorporation of spatial variability in sea-level associated with each component. The summation we use is the same as Grinsted et al. (2015) where the time dependent global average projection for each component (e.g. Glaciers: $GLA(t)$) is multiplied by its associated fingerprint (e.g. $F_{GLA}(\theta,\phi)$) and then aggregated to give,

$$\begin{aligned} RSL(\theta,\phi,t) = {} & F_{SAL}(\theta,\phi)\cdot[STR(t) + DSL(\theta,\phi,t)] + F_{GLA}(\theta,\phi)\cdot GLA(t) \\ & + F_{GRE}(\theta,\phi)\cdot GRE(t) + F_{ANT}(\theta.\phi)\cdot ANT(t) \\ & + F_{LW}(\theta,\phi)\cdot LAN(t) + GIA(\theta,\phi)\cdot t + TECT(\theta,\phi,t) \\ & + NCLIM(\theta,\phi,t). \end{aligned} \quad (1)$$

The contributions in (1) are, the impact of self-attraction and loading (SAL) of the ocean upon itself due to the long term alteration of ocean density changes, globally averaged steric sea-level rise (STR), dynamic sea-level change (DSL), glaciers and ice-caps (GLA), Greenland ice sheet (GRE), Antarctic ice sheet (ANT), land-water storage (LAN), Glacial Isostatic Adjustment (GIA), tectonics (TECT) and non-climatic land-motion (NCLIM). The last two terms (TECT and NCLIM) represent the local effect of non-GIA and environmentally induced land motion respectively. Since these terms are difficult to quantify as global fields at present and even more difficult to forecast through the century, we omit them from our projection. The fingerprints in (1) represent the ocean surface response to the mass redistribution of a given component. For example, land-based ice masses (GLA, GRE, ANT) gravitationally attract the oceans surrounding them whilst changes in these masses alter the elastic solid earth instantaneously thus perturbing Earth's rotation (Milne and Mitrovica, 1998a). The interaction of these mechanisms results in a unique equipotential (ocean) surface for each component. The sea-level fingerprints described here have been calculated by solving the sea-level equation (Farrell and Clark, 1976), following a pseudo-spectral approach (Mitrovica and Peltier, 1991), and including changes in the Earth's rotation (Milne and Mitrovica, 1998a) and the effects of migrating coastlines (Milne and Mitrovica, 1998b). The elastic response of the solid Earth has been computed for a radially stratified and compressible Earth based on the Preliminary Reference Earth Model (Dziewonski and Anderson, 1981). All of the sea-level fingerprints described below were computed and supplied by R. Riva (TU Delft), with the exception of GIA.

2.1. Global mean sea-level components

Each GMSL component has a time dependent median projection with uncertainty bounds defined for each scenario.

In the case of RCP 4.5 and RCP 8.5 scenarios GMSL components GLA, GRE, ANT and LAN are taken from IPCC AR5 (Church et al., 2013). We calculate STR directly using outputs from CMIP5 (Section 2.3). Each component is defined by a median and 'likely' range (17th to 83rd percentiles) sampled yearly throughout the 21st century relative to the average of 1986–2005 (Fig. S1).

The High-end scenario uses the total GMSL projection of Jevrejeva et al. (2014) at 2100 relative to 2000. Jevrejeva et al. (2014) calculated total GMSL by using projections of STR, GLA and LAN for RCP 8.5 from IPCC AR5 (Church et al., 2013) and projections of GRE and ANT from the expert elicitation of Bamber and Aspinall (2013), which have large uncertainties in their right-hand tails. Whilst the High-end scenario's median GMSL rise (0.80 m) is close to IPCC AR5 RCP 8.5 (0.74 m, Church et al., 2013), the 95th percentile (5% probability) GMSL is 1.80 m compared to 1.21 m. We extrapolate the GMSL High-end projection for each component at median, 5th and 95th percentiles (Fig. S1) using standard linear least-squares across the 21st century by assuming that the acceleration of sea-level rise is constant through the century and that the present-day rate is defined by Church et al. (2013).

2.2. Sea-level fingerprint components

The provenance of each sea-level fingerprint is as follows. F_{GLA}, F_{GRE} and F_{ANT} are from Bamber and Riva (2010), who calculated them from estimates of mass-change in each land-ice component derived from satellite gravimetry and synthetic radar aperture interferometry for the period 2000–2008. In the resulting fingerprints (Fig. S2a–c) F_{GRE} shows a RSL fall along the Atlantic coastlines of Europe and Canada and a far-field rise around South America (e.g. Mitrovica et al., 2011). F_{ANT} shows a RSL fall close to the West Antarctic ice sheet and southern tip of South America and a RSL rise everywhere else. F_{GLA} shows a small contribution to RSL in the far-field whilst a local RSL fall occurs close to glacier sources.

F_{LAN} (Fig. S2d) is calculated using projected changes in land water storage from Wada et al. (2012) who used a flux-based method to estimate the difference between groundwater extraction and recharge for various climate scenarios with transient climate forcing from three General Circulation Models (ECHAM, HadGEM1, HadGEM2).

F_{SAL} (Fig. S2e) is calculated to account for the redistribution of ocean mass from the deep ocean interior to shallow coastal regions as a result of volumetric expansion (Landerer et al., 2007). Mass-changes were estimated using projected ocean bottom pressure change from NorESM1-M and normalised (Richter et al., 2013). The fingerprint is then used to scale the local change in the sum of STR and DSL, which is an approximation that only holds if the mass redistribution used to calculate F_{SAL} is from the same emission scenario (Grinsted et al., 2015).

A critical assumption to using Eq. 1 to make RSL projections is that each fingerprint is time invariant. That is to say the spatial pattern of mass change for each component remains the same through time. This is pertinent for glaciers and ice sheets given their possible large contribution to future sea-level rise.

For glaciers, the assumption infers that the ratio of melt from one glaciated region to another will remain constant over the century. We validated this assumption by studying projected sea-level contributions from 19 glacial regions for RCP 4.5 and RCP 8.5 (Marzeion et al., 2012). We calculated the ratio of regional to global glacier contribution through time and found that ratios of 12 (RCP 4.5) and 11 (RCP 8.5) glacial regions varied by less than ±1% during the 21st century (Fig. S3). The ratios of other regions increase by up to 5% (e.g. Alaska). We considered the uncertainty of contributions for each glacial region (Marzeion et al., 2012) and found that those regions whose ratio exceeded ±1% variability had uncertainty ranges overlapping this threshold (Fig. S3). These small percentage changes allow us to assume a fixed ratio of melt and thus a single global glacial fingerprint. Some of the uncertainty postulated by this analysis is implicit in the ranges for the GLA GMSL components, which incorporated results from Marzeion et al. (2012) (Church et al., 2013).

In the case of ice-sheet variability, we consider that the pattern of future ice-mass loss will lie between present-day and uniform end-members for different scenarios (DeConto and Pollard, 2016). Tamisiea et al. (2010) showed differences in fingerprints due to these end-member states for a mass loss equivalent of 1 mm year^{-1} GMSL rise. Extrapolating RSL rates for a 100 year period shows uncertainties might be up to

1 cm and ≥10 cm for sites distant from and close to centres of mass loss. We explore the impact of ice-sheet uncertainty in our discussion.

In addition to the mass components that contribute to RSL, GIA contributes to present-day sea-level with a spatial pattern that can be assumed constant over the 100 year time scale. We use the ICE-6G_C (VM5a) deglaciation model (Fig. S2f; Peltier et al., 2015), which shows the visco-elastic effect of the deformation of the solid Earth upon sea-level caused by the ice-ocean mass redistribution during the last deglaciation.

2.3. Steric and Dynamic Sea-level components

2.3.1. Data from the CMIP5 archive

We use five output variables from CMIP5 (Table S1): the globally averaged steric sea-level (STR, also ZOSSGA in CMIP5) due to thermal expansion and saline contraction, sea-surface height (ZOS in CMIP5) defined as the local height from the global mean (Landerer et al., 2014) caused by ocean circulation due to surface momentum and buoyancy fluxes (Yin et al., 2010), atmospheric pressure and water content (PSL and PRW in CMIP5 respectively) to calculate the inverse barometer (IB) correction (small compared to ZOS). We also use outputs for sea-ice thickness and extent for two models (MIROC5 and GISS-E2-R; Yin, 2012) in order to correct sea-surface height at high-latitudes. We calculate equivalent sea-level anomalies for sea-surface height, PSL and PRW so that the global mean at each time slice is zero. The net dynamic sea-level (DSL) is then sea-surface height corrected for the IB effect.

We chose to use all available models and model members for each variable. For example, we use 34 (94 members) and 33 (83) models for sea-surface height (RCP 4.5 and RCP 8.5 respectively) compared to 20 (1) for Perrette et al. (2013), 21 (1) for Slangen et al. (2014a), 12 (1) for Grinsted et al. (2015), 24 (1) and 29 (1) (RCP 4.5 and RCP 8.5 respectively) for Kopp et al. (2014).

2.3.2. Drift corrections

Our first processing step is to correct the output variables for model uncertainty, which occurs because different models yield different responses to the same external forcing as a result of differences in, for example, physical and numerical formulations (Deser et al., 2012; Little et al., 2015). This uncertainty is manifested in each variable drifting through time, particularly those that are ocean-based. The integrated effect of drift upon sea-level change may considerably bias projections at the regional level (Sen Gupta et al., 2012, 2013). We correct the historical (1850–2005) and projected (2006–2100) parts of each variable using linear regression from the full-length pre-industrial control run of each model member. The relatively linear drift occurring in the steric component of most models may come about through a constant energy leak (Lucarini and Ragone, 2011). For gridded parameters, we apply the same linear drift correction to each grid node independently.

2.3.3. Multi-model ensemble mean

We follow the method described by Yin (2012) to calculate the multi-model ensemble mean (MEM) and standard deviation of each variable (described in Supplementary Materials). STR is calculated yearly until 2100 and DSL components (ZOS, PSL, PRW) are averaged over 20 years in 10 year time slices (e.g. 2090: 2080–2100) relative to the reference period (1986–2005) except 2100, which is simply the MEM at that time relative to the reference period. DSL components of each model are interpolated onto a $1^\circ \times 1^\circ$ grid (e.g. Slangen et al., 2014a) prior to calculating their MEM and standard deviation. The method assumes that all available models carry equal weight, regardless of the number of members within a given model.

We also calculated MEM projections for STR using one member from each model and found negligible differences between these results and those using all members. A visual comparison between projected STR + ZOS components with Slangen et al. (2014a) at 2081–2100 for RCP 4.5 and 8.5 shows remarkable similarity, both spatially and in terms of magnitudes. The addition of multiple members to the ZOS component appears to reduce the standard error of STR + ZOS by ~2 cm over the century in the Indian Ocean (RCP 4.5) and give a more systematic reduction (~2–3 cm) over the century for RCP 8.5.

An interesting question to pose at this point is whether the MEM and standard deviation are appropriate statistical measures for these ensembles. Fig. S1e–f shows the suite of model outputs for STR and the associated MEM and 2 sigma uncertainties. At each time slice, we perform a K-S test for normality (Massey, 1951) and find that STR supports the null hypothesis that the distribution of models is drawn from a standard normal distribution at the 95% confidence level. We apply the same test to DSL components (ZOS, PSL, PRW) and find distinct regions, which also vary with time that do not support the null hypothesis. Fig. S4a,g shows the p-value of the K-S test at each grid point of ZOS for RCP 4.5 and RCP 8.5 at 2090 respectively. Regions where the p-value falls below 0.05 show model ensembles that do not support the null hypothesis. For ZOS the north-eastern Pacific (Fig. S4b,h), central-eastern Pacific, central-eastern Atlantic and patches of the Indian Ocean show p-values close to or below the threshold. It was pointed out by Little et al. (2015) that outlier models within the ensemble appeared to have stronger atmospheric feedbacks, which drove a decline in ocean circulation and enhanced upper-ocean warming. The Mediterranean Sea and Hudson Bay (Fig. S4c,i) also contain non-Gaussian distributions of ensembles, which can be attributed to poor handling of inland and semi-enclosed seas by certain GCM/Earth-System models. To estimate the effect of asymmetry in model ensembles upon projected ZOS, we calculate the difference between 2 standard deviation ensemble range (assuming MEM) and the equivalent 2.5th - 97.5th percentiles (assuming the ensemble represents a PDF). Differences in these uncertainty ranges in regions of the open ocean that fail the null hypothesis are on average 20 mm by 2090 for both RCP scenarios. Hudson Bay/Mediterranean Sea regions show differences of −19/120 mm and −24/112 mm for RCP 4.5 (Fig. S4d) and RCP 8.5 (Fig. S4j) respectively. We correct for the skew at each grid point by removing outlier model values using the generalised extreme Studentized deviate test (Rosner, 1983), and then recalculate mean, standard deviations, K-S tests and percentiles. After the corrections, regions that did not support the null hypothesis disappear almost everywhere (Fig. S4e,k). The differences in uncertainty ranges for the formerly skewed regions in the open ocean are on average reduced to 4 mm and 2 mm, whilst differences in Hudson Bay/Mediterranean Sea are reduced to 3/30 mm and 20/60 mm for RCP 4.5 (Fig. S4f) and RCP 8.5 (Fig. S4l) respectively.

2.3.4. Comparison to observations

We compared the MEMs of sea-surface height anomalies and atmospheric pressure sea-level equivalent anomalies to observations (1993–2006) of the same and found that differences are less than ±20 mm over much of the global oceans (Figs. S5–S7). The similarity between the spatial patterns and amplitudes between models and observations reveal the ability of each component from the models used to compute DSL and atmospheric pressure to reproduce dominant stationary features. The equal-area global root mean square difference (GRMSD) for time-mean DSL anomaly and sea-level equivalent atmospheric pressure anomaly are both 16 mm, whilst equal-area GRMSD for standard deviations of these anomalies are 13 mm and 2 mm respectively. Regions where differences exceed this range coincide with areas of strong sea-level gradients. Since the CMIP5 models are not eddy permitting (excepting MIROC4h), smoothed patterns occur over ocean regions that display strong local dynamics and currents in the altimetry thus causing strong differences (e.g. central Pacific and Weddell Sea gyre) along with southward shifts of those deviations (e.g. Kuroshio and Agulhas currents). Our DSL inter-comparison is supported by Landerer et al. (2014) who found the MEM GRMSD between DSL measured above the geoid and mean dynamic topography is ~9 mm (1992–2002). Similarly our atmospheric pressure inter-comparison is supported by Stammer and Hüttmann (2008) who found good first order agreement

between observed atmospheric components and a single GCM, whilst the attribution study by Slangen et al. (2014b) found the MEM global average thermosteric trends captured the observed data for the second half of the 20th century by using anthropogenic and natural forcing. These comparisons show that confidence can be given to MEMs of CMIP5 variables to represent the ocean-atmosphere system well and thus may be extended to RCP scenarios.

2.4. Scaling and summation of sea-level components

We now have all the relevant components in Eq. 1 to derive RSL projections. Firstly, we derive a PDF for each global mean sea-level component (GLA, GRE, ANT, LAN) at each time slice using the three percentiles described for each scenario. To do this we employ a forward model of the Burr distribution (Burr, 1942; Tadikamalla, 1980), a highly flexible PDF that can express a wide range of shapes,

$$f(x|\alpha,c,k) = \frac{\frac{kc}{\alpha}\left(\frac{x}{\alpha}\right)^{c-1}}{\left(1+\left(\frac{x}{\alpha}\right)^{c}\right)^{k+1}} \quad (2)$$

where α is the scale parameter and c, k are shape parameters (x; α; c; k > 0). We search over α, c and k using the Nelder-Mead simplex method (Lagarias et al., 1998) to create a PDF whose distribution minimises the root-mean squared (RMS) misfit between modelled and 'observed' percentiles (p-value$_{RCP4.5/RCP8.5}$: 0.17, 0.5 and 0.84, and p-value$_{High\text{-}end}$: 0.05, 0.5, 0.95) for each component at each time slice. Since the Burr distribution requires x > 0, we shift the GSL (for each component) given at each percentile by a fixed amount prior to calculating the forward model. Fig. 1 shows an example of the resulting PDFs, whilst Table S2 shows small time-averaged RMS misfit for each component.

We randomly sample each PDF 1000 times then subtract the fixed amount from the realisations to shift them back to satisfy the original percentiles. Secondly, we use the realisations of GSL for each component and scale them by the associated normalised fingerprint (F_{GLA}, F_{GRE}, F_{ANT}, F_{LAN}). Thirdly, we randomly sample each of the CMIP5 MEM sea-level components (DSL and STR) 1000 times using the mean and standard deviations calculated after the removal of outlier models as described in Section 2.3.3. GIA is independent from climate scenarios thus the fingerprint (F_{GIA}) is scaled by the time relative to the reference period, and does not include any uncertainty (see discussion). Fourthly, we sum one realisation from each component and repeat for all realisations to give 1000 realisations of total projected RSL at each time slice for each scenario. This assumes that sea-level components are uncorrelated for all scenarios. Finally, we calculate quantiles from projected RSL realisations at each grid point to explore the probability of likely sea-level change.

3. Results

We show projections of RSL for RCP 4.5, RCP 8.5 and High-end scenarios. Figs. 2, 3 and 4 show, respectively, the median probability (50th percentile), upper 5% probability (95th percentile) and 90% probability range (5th - 95th percentiles) at 2030, 2060 and 2090 relative to 1986–2005. The two contours plotted in each panel show GMSL (black) and zero RSL (white). Early in the century, the RSL projection is consistent across all scenarios (Fig. 2 a–c, and Fig. 3 a–c). From the middle of the century the patterns of RSL for RCP 4.5 and RCP 8.5 (Fig. 2 d–e, 3 d–e) deviate from the High-end scenario (Fig. 2f, 3f) where the Antarctic contribution begins to dominate. This is clearly observed in the pattern of uncertainty (Fig. 4d–e compared to Fig. 4f). By the end of the century the amplitude and pattern of sea-level is clearly distinct for each scenario. At the global scale, the High-end scenario begins to deviate from RCP 4.5 and RCP 8.5 projections between 2030 and 2040. At the 95th percentile, differences between projected GMSL for High-end and RCP scenarios are 3 cm in 2030 rising to 8–9 cm in 2040. By the end of the century, the differences between RCP 4.5 to RCP 8.5 and RCP 8.5 to High-end are 16 cm and 21 cm (median and 95th percentile), and 8 cm and 45 cm (median and 95th percentile) respectively. The range of uncertainty at the end of the century for the High-end scenario (Fig. 4i) is >50 cm larger than that of the RCP scenarios (Fig. 4g–h).

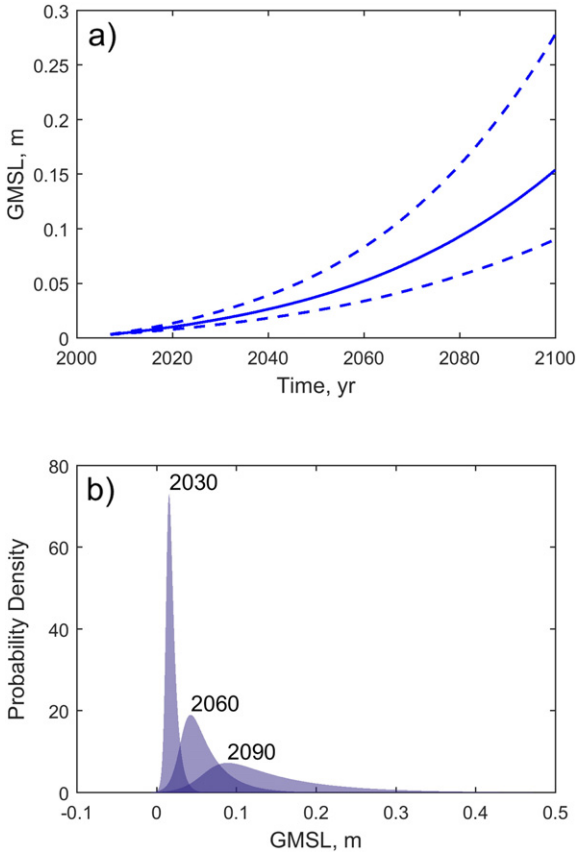

Fig. 1. Construction of PDFs for AR5 RCP 8.5 Greenland component of 21st century sea-level projection. a) GMSL projection at 17th, 50th and 83rd percentiles. b) Continuous PDF's at 2030, 2060 and 2090 calculated using a grid-search algorithm to search for a Burr distribution that fits GMSL values at percentiles in a).

For median probability, areas experiencing a RSL fall are close to the coastlines of Greenland, Alaska, west Antarctica, Gulf of Bothnia and areas of the Barents Sea and Hudson Bay. The primary mechanism driving the fall in RSL varies by location such that GIA affects Hudson Bay, Barents Sea and Gulf of Bothnia, ice-sheet mass loss affects Greenland and Antarctica and glacier loss affects Alaska. Of these regions, only Hudson Bay experiences a RSL fall over the century at the 95th percentile whilst the others show a RSL rise that is less than the global average. The GMSL contour migrates with time. For median probability, all scenarios show an increase in ocean areas where RSL exceeds GMSL of between 11 and 13% (2010−2100).

4. Discussion

4.1. Comparison to earlier studies

Table 1 shows GMSL projections for the three scenarios separated by component and the total, which is not the sum of the components due to the probabilistic method we employ, and publications using similar methods. Our GMSL projections fit the median and likely (17th-83rd percentile) range of AR5 RCP 4.5 and RCP 8.5 within 1 cm. There is strong agreement between the median GMSL projections for these scenarios with Slangen et al. (2014a) and Kopp et al. (2014), whilst the discrepancy with the estimate by Spada et al. (2013) is due to their exclusion of the land-water component (~5 cm by 2100). It is in the

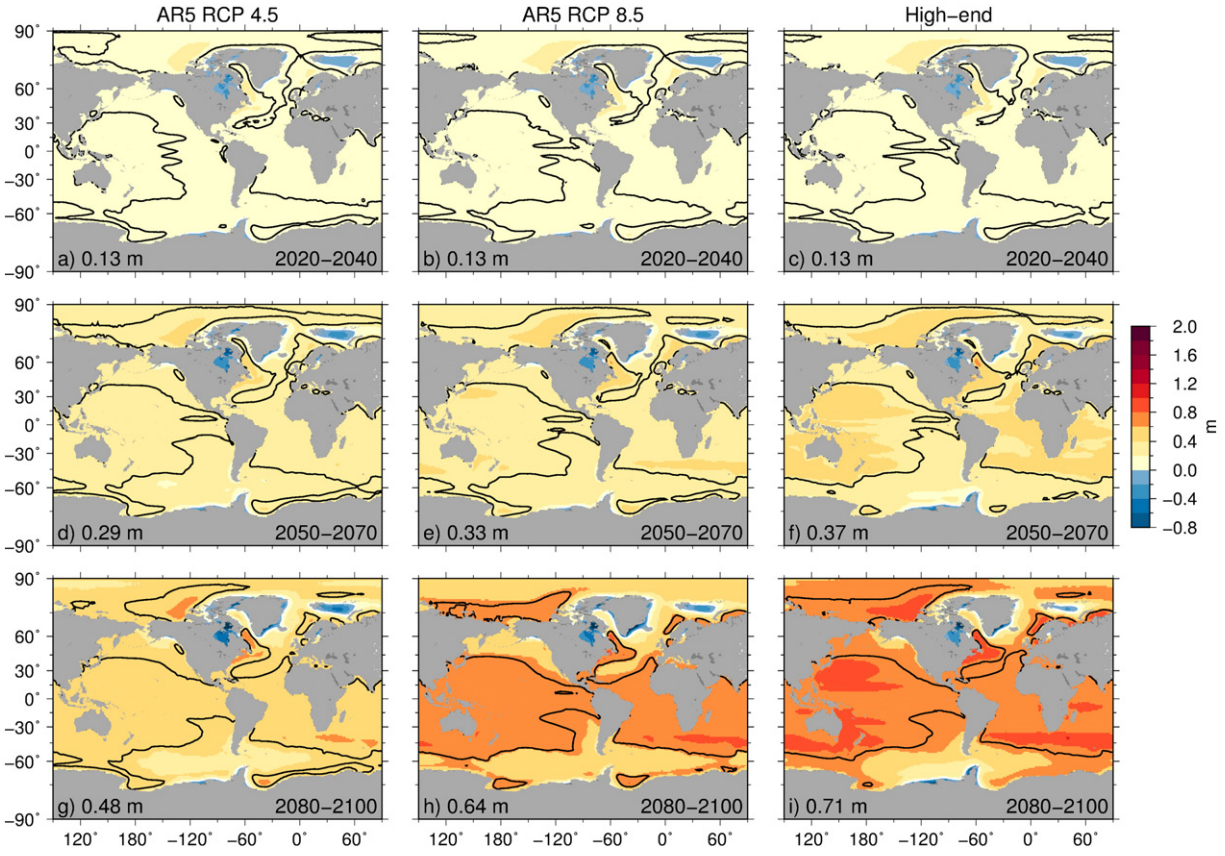

Fig. 2. Projections of median RSL change at 2030, 2060 and 2090 relative to 1986–2005 for scenarios RCP 4.5 (a, d, g), RCP 8.5 (b, e, h) and High-end scenario (c, f, i). Black contour is the median GMSL rise labelled in each panel.

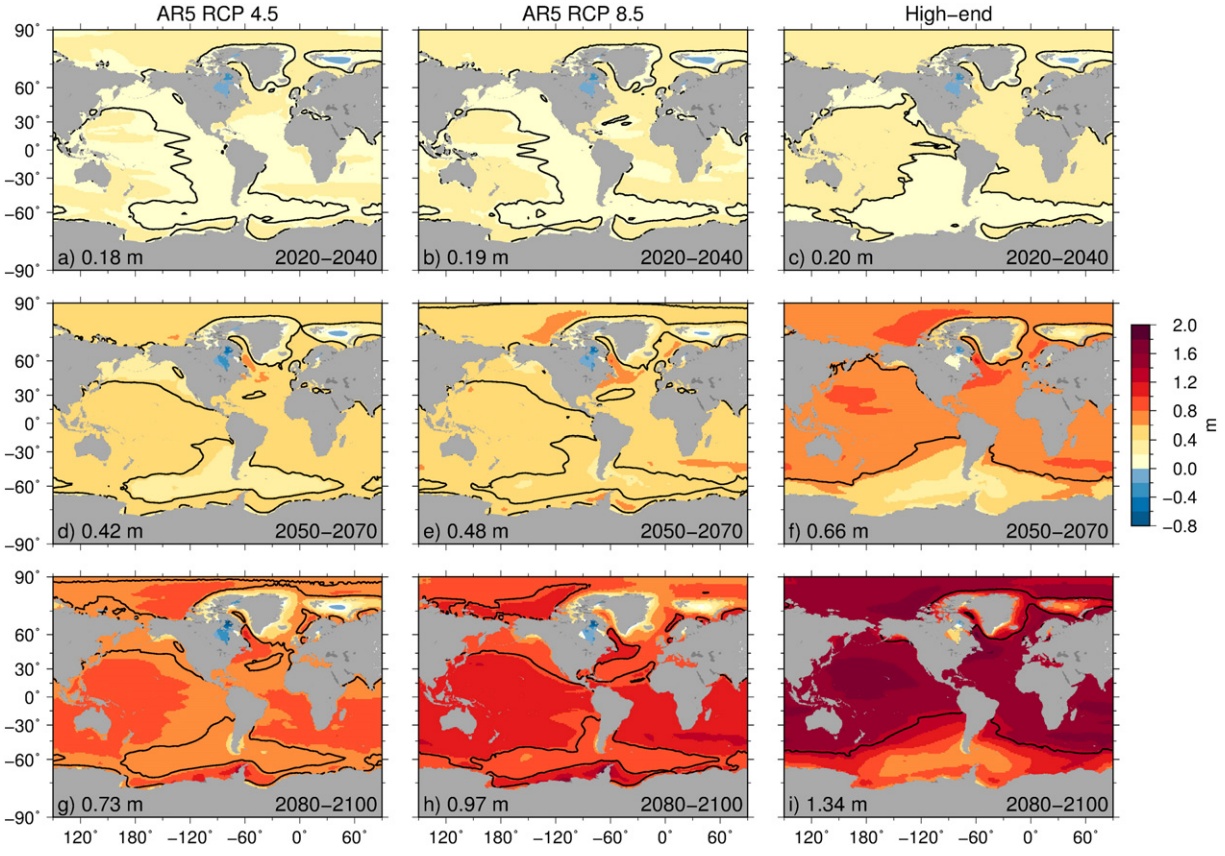

Fig. 3. As in Fig. 2, but for 95th percentile RSL change. Black contour is the 95th percentile GMSL rise labelled in each panel.

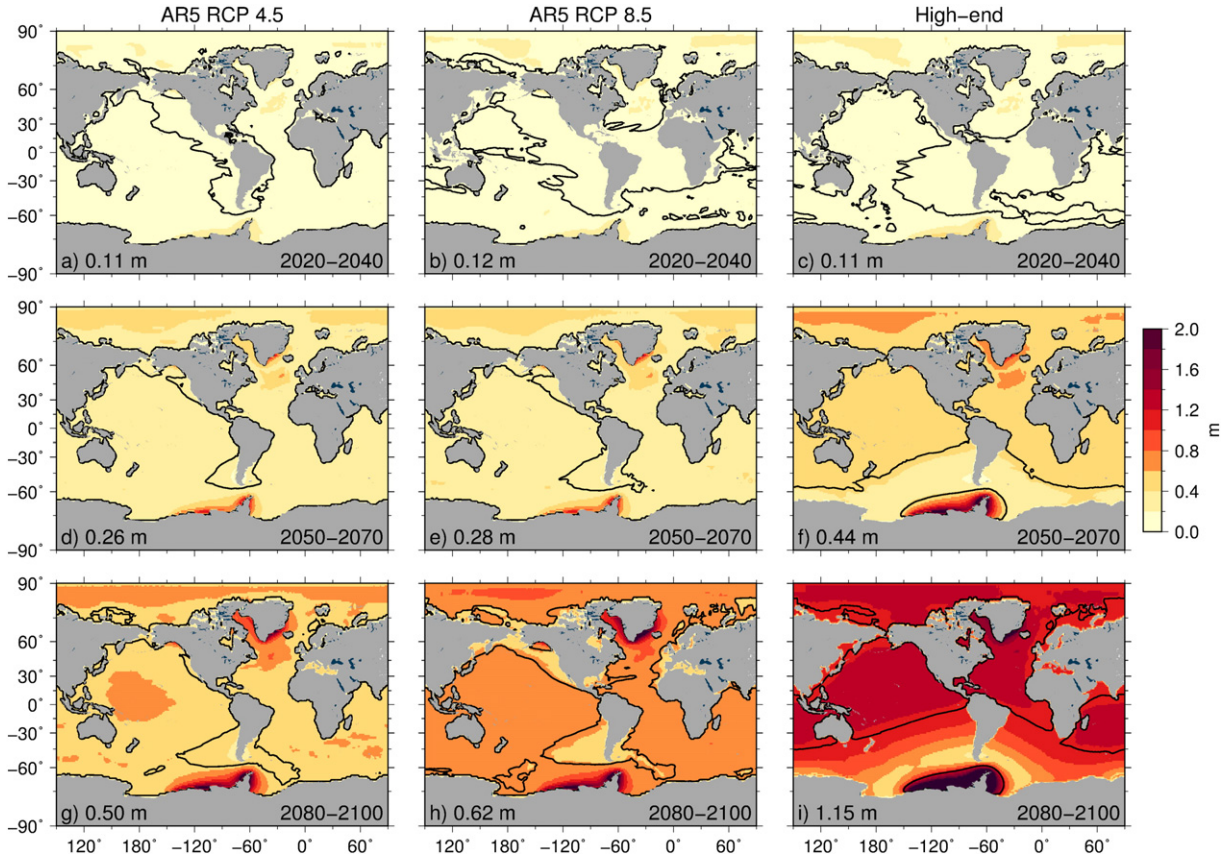

Fig. 4. As in Fig. 2, but for 90% probability range (5th–95th percentiles). Black contour is the GMSL rise 90% probability range labelled in each panel.

tails of the distribution that differences emerge, for example the 17th percentile of RCP 8.5 by Slangen et al. (2014a) is 10 cm less than our projection or AR5 (Church et al., 2013).

Whilst our GMSL projections for each scenario have likely ranges of uncertainty that are similar to Perrette et al. (2013), significant differences occur for median GMSL projections (+15 cm, +19 cm and −22 cm for RCP 4.5, RCP 8.5 and High-end respectively). These differences are due to our inclusion of a land-water component and to the size of Greenland and Antarctic contributions compared to those we use. Contributions are smaller in Perrette et al. (2013)'s projections for RCP 4.5 and RCP 8.5 but larger in their RCP 8.5 "semi-empirical" (High-end) scenario. The spatial patterns of our RSL projections are similar to Perrette et al. (2013) and Slangen et al. (2014a), where the location and relative magnitude of enhanced and reduced sea-level rise and the location of GMSL contours are consistent.

The High-end projection we present agrees well with Grinsted et al. (2015) across the PDF of GMSL, except in the right-hand tail where the difference at 95th percentile is 16 cm. This is likely due to two assumptions. First, we assume that sea-level components are uncorrelated, which may be of importance to the ice-sheets, and second, the use of a single fingerprint for Antarctica which imposes a fixed relationship between mass loss in West and East Antarctica. These assumptions are

Table 1
GMSL projections at 2100 by component and total for this study and total for publications using similar methods.

	RCP 4.5				RCP 8.5				High-end			
cm	50	17–83	5–95	99	50	17–83	5–95	99	50	17–83	5–95	99
2100 - components												
Glaciers	13	7–21	1–27	35	18	10–27	4–35	45	18	11–26	5–32	38
Greenland	9	6–15	3–23	36	16	9–27	6–42	69	14	10–23	8–33	51
Antarctic	5	−5–15	−15–22	33	3	−7–14	−19–21	32	12	−3–46	−7–94	166
Steric	21	16–26	11–30	36	32	25–39	19–45	53	32	26–38	20–42	47
Land-water	5	−2–11	−7–15	23	4	−2–11	−7–15	23	4	0–9	−4–14	21
Total	54	36–72	22–85	100	75	54–98	37–118	140	84	63–121	51–167	222
Other projections in 2100												
AR5	53	36–71			74	52–98						
S13[a]	50								100			
P13	39	31–49			56	44–70			106	78–143		
K14[b]	59	45–77	36–93	147					79	62–100	52–121	176
S14a	54	35–73			71	43–99						
G15									80	58–120	45–183	

AR5: Church et al. (2013), S13: Spada et al. (2013), P13: Perrette et al. (2013), K14: Kopp et al. (2014), S14a: Slangen et al. (2014a); G15: Grinsted et al. (2015).
[a] S13 uses "mid –" and "high –" end projections of land-ice mass loss with the SRES A1B ocean dynamic component.
[b] K14 present 99.5th percentiles for RCP 4.5 and RCP 8.5 scenarios – their RCP 8.5 is equivalent to our High-end.

linked because Bamber and Aspinall (2013) ascribe correlations between Greenland, West and East Antarctica to formulate their PDF for global ice-sheet contribution to sea-level. Using different inter-ice sheet correlations, including an uncorrelated case, Bamber and Aspinall (2013) found a minimal impact on the median but some effect on the upper tail of the PDF. This impact upon the right-hand tail supports the difference between our High-end GMSL and Grinsted et al. (2015) at the 95th percentile. The effect of this difference upon projected RSL varies spatially and is dependent upon the magnitude of each fingerprint at a given location. For example, in north-west Europe, the Greenland fingerprint is close to zero (Fig. S2b), thus covariance between ice-sheet components becomes unimportant.

Our High-end projection agrees closely with the median, 5th and 17th percentiles for RCP 8.5 by Kopp et al. (2014). However the 83rd, 95th and 99th percentiles differ by 21 cm, 46 cm and 46 cm respectively by 2100. The differences, again in the right-hand tail occur because of Kopp et al. (2014)'s use of correlation between sea-level components, and the way Kopp et al. (2014) merge the PDF tail structure from Bamber and Aspinall (2013) with the median and likely range of AR5 RCP 8.5. In contrast with the second point, we follow Jevrejeva et al. (2014) and Grinsted et al. (2015) by using the PDFs of Bamber and Aspinall (2013) as they are, simply substituting them for those of AR5 (Oppenheimer et al., 2016).

We explore the spatial variability between our High-end and Kopp et al. (2014)'s RCP 8.5 projections by comparing the climatically driven sea-level change (omit land-water and uplift terms from equation 1) of each at 2100. We calculate the ratio of climatically-driven RSL to GMSL (scale factor R, Kopp et al., 2014) for each projection at a subset of global tide gauge locations and present the differences at median probability (Fig. 5). To improve the inter-comparison, we made our RSL projection using Greenland and Antarctic fingerprints calculated from uniform patterns of ice-mass loss (note that Kopp et al., 2014 in fact use separate fingerprints for East and West Antarctica, though a further inter-comparison is beyond the scope of this study). Differences in the scale factor lie between 0 and 0.2 for much of the global coastlines suggesting that for the same global sea-level rise, our High-end scenario projects higher RSL rises than Kopp et al. (2014). Furthermore, regions with strong differences in scale factor are in close proximity to glacial regions (Alaska, Northern Canada and North Russia) whose projected contribution changes by more 3% over the century (Fig. S3). The differences along the North American west coast are due to the negative portion of our glacial fingerprint reaching much further south than Kopp et al. (2014).

As Kopp et al. (2014) discussed, the maximum sea-level rise in the 21st century has been theorised at 2.0 m (Pfeffer et al., 2008), 2.25 m (Sriver et al., 2012) and 2.7 m (Miller et al., 2013). These upper limit estimates differ because of their relative estimates of land-ice sea-level contributions and globally averaged steric sea-level; the upper limit of Miller et al. (2013) corresponds to the 99th percentile of our High-end scenario GMSL PDF at 2100 relative to 1986–2005.

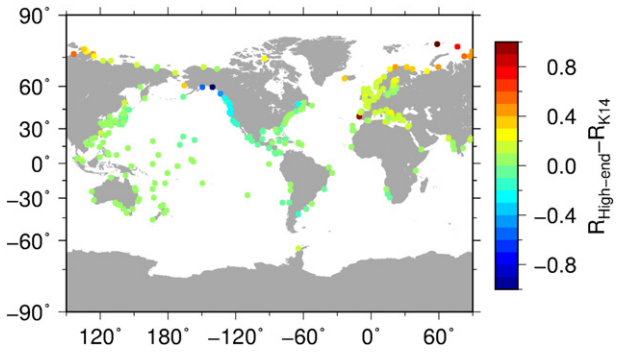

Fig. 5. Difference between scale factors (ratio of RSL to GMSL) of climatologically driven RSL projections at 360 tide gauge locations for our High-end projection and Kopp et al. (2014) at 2100.

4.2. Uncertainty in CMIP5 analysis

As described in Section 2.3.1, we correct internal variability for each CMIP5 model variable using linear regression of the control run. Slangen et al. (2014a) and Grinsted et al. (2015) performed drift corrections by analysing control runs using respectively, 2nd and 1st (DSL)/2nd (thermo-steric) order polynomial fits. Whilst Kopp et al. (2014) do not describe how, or if, they correct DSL for drift, the correction for thermo-steric sea-level adjusts each model output so that over the period 1861–1900 its rate matches the average GMSL rate corrected for glacier mass loss over the same period. The resulting difference in projected thermos-steric sea-level change with AR5 RCP 8.5 (Church et al., 2013) by 2100 is 6, 1 and 9 cm for median, 5th and 95th percentiles respectively (Fig. S8). We compared steric projections using linear, quadratic and cubic drift corrections and found that differences are <2 cm over the century (Fig. S9) with the exception of models MIROC-ESM and MIROC-ESM-CHEM. This is supported by Sen Gupta et al. (2013) who suggest using the full pre-industrial control run of each model to calculate linear, quadratic or cubic polynomials for drift corrections.

To check the effect of drift upon projected DSL, we compare the 21st century projections (relative to 1986–2005 time-average) using the quadratic drift correction to the 21st century projections using the linear drift correction (Fig. S10). Both corrections used the full pre-industrial control run. The majority of differences in MEM projections through the century due to the drift correction lie between −4 and +4 mm. Upon further inspection of individual models (Fig. S11), there are outliers to the MEM that can be on the order of centimetres difference over the 21st century, even for common model groups (e.g. MIROC models: Fig. S11a–c). The different models generally show smaller variability in the mid-latitude ocean regions, though even here regional variability exists (Fig. S11d). Significantly more variability appears in polar regions; Bordbar et al. (2015) point out that projections for the Southern Ocean are likely to be overestimated by current climate models due to their inability to resolve the effect of eddies and the ocean response to wind forcing. Our assessment of CMIP5 uncertainty in terms of drift corrections shows that whilst the impact of drift correction choice is small upon the MEM, internal variability varies widely by location and across models that can lead to differences of several decades in local emergence of RCP forcing above the non-anthropogenic background (Little et al., 2015). As we showed in Section 2.3.3, individual models of the ensemble may also qualify as outliers to the MEM at each grid point (Fig. S1) and that treating the ensemble as a continuous PDF rather than a Gaussian distribution results in differences between projected sea-levels an order of magnitude larger than the choice of drift correction.

4.3. Uncertainty in land-ice contribution

The RSL projections show the importance of the ice sheet contribution, so it is relevant to consider the cause and possible variability in the spatial pattern of ice-mass loss. Whilst the mass balance of the Greenland ice sheet has increased due to surface runoff (Ettema et al., 2009) and localised ice discharge (Rignot et al., 2010; Moon et al., 2012), it had been thought that the Greenland ice sheet's susceptibility to ocean warming was limited due to its topography (Pfeffer et al., 2008). However, recent bathymetric surveys showing deeper than previously measured glacial fjords indicate that warm, salty Atlantic waters with high melt potential can reach glacier fronts thus requiring altered estimates of present and future melt potential (Rignot et al., 2016) and hence Greenland's potential sea-level contribution.

In contrast to Greenland, the Antarctic ice sheets have large grounded ice flows discharging into floating ice shelves, creating the conditions for marine ice-sheet instability (MISI; e.g. Bamber et al., 2009; Mitrovica et al., 2009; Pollard et al., 2015). This extreme situation is not represented in the AR5 RCP scenarios, which have conservative contributions to the global average by the end of the century (Table 1). Recent advances

in dynamical solid-ice and surface-mass balance models projecting Antarctic ice sheet loss continue to give median sea-level equivalent (SLE) rises within the range of RCP scenarios though variances are up to three times smaller than the High-end scenario at 2100. Studies by Little et al. (2013), Levermann et al. (2014) and Ritz et al. (2015) project 95th percentile Antarctic SLE by 2100 of 13 cm, 27 cm and 37 cm (RCP 4.5 and RCP 8.5), and 30 cm (SRES A1B, Nakićenović and Swart, 2000) respectively.

However, these studies also state that mechanisms such as onset of MISI (Ritz et al., 2015), inter-basin spatial correlation (Little et al., 2013; Albrecht and Levermann, 2014), abrupt calving, ice melt – ocean circulation feedbacks and self-amplification of grounding line motion are difficult to model and are likely to play important roles in ice mass loss from Antarctica. Indeed at their limits, these three studies posit GMSL contributions up to 40 cm (95th percentile, Little et al., 2013), 60 cm (1 uncalibrated model, Ritz et al., 2015) and 54 cm (95th percentile using RCP 8.5 and zero ice-ocean time delay-feedback, Levermann et al., 2014). Pollard et al. (2015) and DeConto and Pollard (2016) incorporated two dynamical mechanisms (atmospherically driven hydrofracturing and ice cliff failure) into an ice sheet model to explore the impact upon projected ice-mass loss for RCP scenarios and found SLE rises of 49 ± 20 cm and 105 ± 30 cm for RCP 4.5 and RCP 8.5 respectively by 2100 (or 26 ± 28 cm (RCP 4.5) and 64 ± 49 cm (RCP 8.5) in an alternative set-up). The modelling advances above illustrate the complimentary value of the High-end projection but that at present the associated variance cannot be reduced: the extended right-hand tail may in fact have a higher probability of occurring than is presented in this study.

Uncertainty also results from making projections using fingerprints of land-ice mass loss that are based upon modern observations and that we assume to be invariant through time. One approach to explore this uncertainty is to see how RSL projections differ when using fingerprints for the ice sheets with uniform patterns of mass loss (Fig. S12, e.g. Tamisiea and Mitrovica, 2011). For most of the century in all scenarios differences are less than ±5 cm both at median and 95th percentiles (Fig. S13–14), which is minimal given the relative contributions of the other land-ice components. Significant differences emerge from 2060 in the High-end scenario, increasing to −45 cm (Southern South America) and +50 cm (Southern Ocean) by 2100 at the 95th percentile. In this situation, the United States, Southern Australia and Southern Africa experience smaller projected RSL (up to 15 cm) for a uniform pattern of ice-mass compared to a realistic pattern (Fig. S14f,i), whilst Southern South America experiences a larger projected RSL (up to 45 cm) for a uniform pattern of ice-mass loss compared to a realistic pattern.

4.4. Uncertainty due to glacial isostatic adjustment

Numerical models for GIA have developed from the seminal work of Farrell and Clark (1976) (e.g. Lambeck et al., 2003; Mitrovica and Milne, 2003; Spada and Stocchi, 2007; van der Wal et al., 2013) and are complimented by models for deglaciation (e.g. ANU, Lambeck et al., 2002; ICE-5G (VM2), Peltier, 2004; ICE-6G_C (VM5a), Peltier et al., 2015). The differences between these models lie in their formulation: that there are 1D or 3D visco-elastic GIA models and simultaneous inversions for earth structure and time variable ice volumes. We use the present-day GIA field calculated from ICE-6G_C (VM5a) (Peltier et al., 2015) and while differences between this and ICE-5G (VM2) (Peltier, 2004) are <0.2 mm year^{-1} for the bulk of the global oceans, they exceed ±1 mm year^{-1} reaching −7 mm year^{-1} and +6 mm year^{-1} in high-latitude regions focused at the former centres of deglaciation (Fig. S12: North America, Scandinavia/Barents-Kara Sea and Antarctica). Assuming the RSL rate due to GIA is constant during the 21st century and that the differences between ICE-5G and ICE-6G_C represent spatial uncertainty, projected RSL change by 2100 would differ by <2 cm in the global oceans, but by up to −70 cm and +60 cm along the North Canadian, Scandinavian and Antarctic coastlines.

4.5. Regional variability in uncertainty

Fig. 4 shows the spatial variability of uncertainty in projected RSL change. The method of aggregating sea-level components we have used also implies that the relative contribution of individual components varies in space and through time. We calculated the fraction of each components variance to the total variance for the three scenarios in the global average and at each grid point (Fig. 6 and Figs. S15–S16). Many of the features shown at the global scale are reflected in the spatial patterns including, the increasing importance of uncertainty in ice-sheet contributions and the falling proportion of Glacier, DSL and Steric uncertainty for all scenarios to a greater or lesser degree. In Arctic, DSL dominates for all scenarios, whilst in the tropics its uncertainty drops towards zero.

In addition to the regional variability of projected uncertainty, additional sea-level components not considered here have the potential to alter projected changes and widen local uncertainty further. First, the impact of shallow ocean dynamics upon coastal sea-level has not been considered because resolution and local scale shoreline complexity is yet to be implemented in coupled atmosphere-ocean or earth system models.

Second, local land movement due to tectonics, sedimentation and environmentally induced subsidence (e.g. ground-water extraction in cities) is not included in our projections. The variability of local effects can be significant: Deltares (2013) showed present-day rates of megacity subsidence for Jakarta, Bangkok and Ho Chi Minh City of 75–100 mm year^{-1}, 20–30 mm year^{-1} and up to 80 mm year^{-1} respectively and total projected subsidence by 2025 of 1800 mm, 190 mm and 200 mm respectively. Assuming these to be realistic, projections made in this paper at these locations and others where strong local uplift/subsidence is occurring are underestimated by tens of centimetres. Equally, projections which seek to account for local land movement (e.g. Kopp et al., 2014) may be similarly uncertain. An example of this from the 20th century is Tokyo (Kaneko and Toyota, 2011), which subsided around 4 m from 1900 to 1975 due to groundwater extraction. The introduction of regulatory measures taken in the 1960′s resulted in a halt to subsidence after 1975. The time varying behaviour of local movement is one that in our opinion is too problematic to apply globally: Kopp et al. (2014) restrict themselves to tide gauge locations, rather than a continuous global field.

5. Conclusions

We have constructed relative sea-level (RSL) projections for the 21st century for three climate change scenarios using a method that aggregates spatial patterns of sea-level components. The probabilistic approach we have taken gives results at median probability for RCP 4.5 and RCP 8.5 that are similar to Perrette et al. (2013), Slangen et al. (2014a) and Kopp et al. (2014). The median projection of the High-end scenario has a magnitude and spatial pattern similar to that of RCP 8.5, however the low-probability (95th percentile), high-impact scenario results in a GMSL of 1.64 m by 2100, which is dominated by the contribution from Antarctica.

We have also considered various aspects of the processing required to construct these projections and found that differences between drift corrections of CMIP5 outputs are small when considering the multi-model ensemble mean (~2 cm per century for steric, 0.5 cm per century for dynamic sea-level [DSL]), but that individual models display much larger variability (e.g. Bordbar et al., 2015; Little et al., 2015). We have shown that the ensemble of models for steric sea-level satisfies the null hypothesis for normality, but for DSL spatially discrete areas occur that fail the null. In fact, differences in projected DSL, between assuming a Gaussian versus continuous (skewed) probability density function, are up to 20 cm (RCP 4.5) and 40 cm (RCP 8.5) at 2 sigma uncertainty for parts of the global oceans.

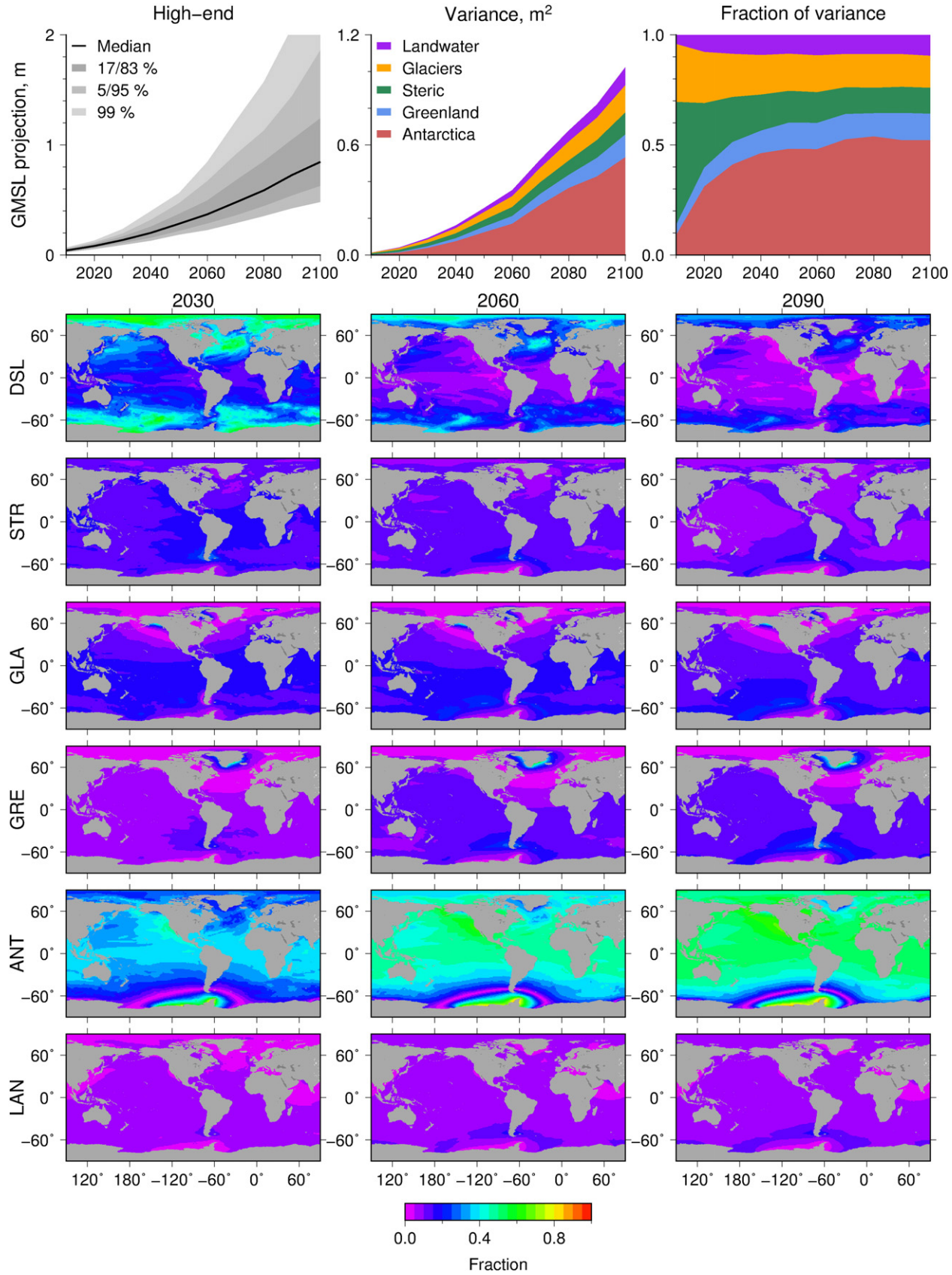

Fig. 6. (Top left) Global projection for High-end scenario, (top middle) Variance of global contributions, (top right) Fraction of variance for global contributions. (Below global projections) Spatial maps for each sea-level component (labelled on left) of fraction of variance at 2030 (left column), 2060 (right column) and 2090 (right column).

The uncertainties associated with the High-end scenario at 2100 are significantly greater than those of the RCP 4.5 and RCP 8.5 scenarios. The 90% range (5th–95th percentile) of projected GMSL by 2100 is 116 cm for the High-end scenario compared to 34 cm and 45 cm for RCP 4.5 and RCP 8.5 respectively. Projected GMSL for the High-end scenario begins to deviate from RCP projections between 2030 and 2040. At the 95th percentile, differences between projected GMSL for High-end and RCP scenarios are 3 cm in 2030, whilst this rises to 8–9 cm in 2040. Recent advances in ice-sheet modelling (DeConto and Pollard, 2016) and bathymetric observation (Rignot et al., 2016) indicate that the projected High-end contributions from Antarctica and Greenland may have a higher probability of occurring than previously thought.

The uncertainty of the total projection is dominated by the contribution from Antarctica, though we have shown that the fraction of each contribution's uncertainty to the total uncertainty varies in time and space (Kopp et al., 2014). Furthermore, we have tested the use of sea-level patterns for realistic and uniform mass loss of Antarctica and Greenland and found that projected differences at the 95th percentile are up to −45 cm (Southern South America) and +50 cm (Southern Ocean) by 2100 though the bulk of the global oceans have cumulative differences of ±4 cm.

Finally, we recognise the limitations of this work: we use spatio-temporally invariant fingerprints that assume fixed melt ratios between globally distributed glaciers and East, West Antarctica and Greenland. We do not include the spatial pattern of steric sea-level change (e.g. Durack et al., 2014) but instead infer the effect of a spatial steric field by using the fingerprint due to ocean self-attraction and loading (Richter et al., 2013 and Grinsted et al., 2015). Additionally, we do not incorporate local tectonic or subsidence effects due to ground water extraction though we do use the global GIA field. Despite these omissions it is clear that much of the global oceans will experience at least the GMSL change projected simply because of the geometry of problem – it is in areas distant from the land-based ice masses and in areas that the oceans can warm the most that sea-level rises are experienced most acutely, which are coincidently the most populous (Hallegatte et al., 2013).

Acknowledgments

This work was funded by the European Union's Seventh Programme for Research, Technological Development and Demonstration under Grant Agreement No: FP7-ENV-2013-Two-Stage-603396-RISES-AM. Satellite altimetry data was accessed from Colorado Sea Level Research Group, http://sealevel.colorado.edu/. NCEP Reanalysis data was provided by the NOAA/OAR/ESRL PSD, Boulder, Colorado, USA, from their Web site at http://www.esrl.noaa.gov/psd/. We acknowledge the World Climate Research Programme's Working Group on Coupled modelling for providing the CMIP5 archive and the climate modelling groups for providing their outputs. Projections from Kopp et al. (2014) were accessed from github.com/bobkopp/LocalizeSL/. We thank Riccardo Riva (TU Delft) for providing fingerprints of sea-level components, GLA, GRE, ANT, LAN and SAL. This paper has been greatly improved by comments from two anonymous reviewers. LPJ is currently working on the Climate Econometrics project, funded by the Robertson Foundation (Grant No: 9907422).

Appendix A. Supplementary data

Supplementary data to this article can be found online at http://dx.doi.org/10.1016/j.gloplacha.2016.10.006.

References

Albrecht, T., Levermann, A., 2014. Spontaneous ice-front retreat caused by disintegration of adjacent ice shelf in Antarctica. Earth Planet. Sci. Lett. 393, 26–30. http://dx.doi.org/10.1016/j.epsl.2014.02.034.

Bamber, J.L., Aspinall, W.P., 2013. An expert judgement assessment of future sea level rise from the ice sheets. Nat. Clim. Chang. 3, 424–427. http://dx.doi.org/10.1038/NCLIMATE1778.

Bamber, J., Riva, R., 2010. The sea level fingerprint of recent ice mass fluxes. Cryosphere 4, 621–627. http://dx.doi.org/10.5194/tc-4-621-2010.

Bamber, J.L., Riva, R.E.M., Vermeersen, B.L.A., LeBrocq, A.M., 2009. Reassessment of the potential sea level rise from a collapse of the West Antarctic ice sheet. Science 324, 901–903. http://dx.doi.org/10.1126/science.1169335.

Bordbar, M.H., Martin, T., Latif, M., Park, W., 2015. Effects of long-term variability on projections of twenty-first-century dynamic sea level. Nat. Clim. Chang. 5, 343–347. http://dx.doi.org/10.1038/NCLIMATE2569.

Burr, I.W., 1942. Cumulative frequency functions. Ann. Math. Stat. 13 (2), 215–232.

Church, J.A., Clark, P.U., Cazenave, A., Gregory, J.M., Jevrejeva, S., Levermann, A., Merrifield, M.A., Milne, G.A., Nerem, R.S., Nunn, P.D., Payne, A.J., Pfeffer, W.T., Stammer, D., Unnikrishnan, A.S., 2013. Climate change 2013: the physical science basis. Contribution of Working Group I to the Fifth Assessment Report of the Intergovernmental Panel on Climate Change, chap. Cambridge University Press, Cambridge, United Kingdom and New York, NY, USA.

DeConto, R.M., Pollard, D., 2016. Contribution of Antarctica to past and future sea-level rise. Nature 531, 591–597. http://dx.doi.org/10.1038/nature17145.

Deltares, 2013. Sinking Cities: An Integrated Approach towards Solutions. https://www.deltares.nl/app/uploads/2015/09/Sinking-cities.pdf.

Deser, C., Phillips, A., Bourdette, V., Teng, H., 2012. Uncertainty in climate change projections: the role of internal variability. Clim. Dyn. 38, 527–546. http://dx.doi.org/10.1007/s00382-010-0977.

Durack, P.J., Wijffels, S.E., Gleckler, P.J., 2014. Long-term sea-level change revisited: the role of salinity. Environ. Res. Lett. 9 (11), 114017. http://dx.doi.org/10.1088/1748-9326/9/11/114017.

Dziewonski, A.M., Anderson, D.L., 1981. Preliminary reference earth model (PREM). Phys. Earth Planet. Inter. 25, 297–356.

Ettema, J., van den Broeke, M.R., van Meijgaard, E., van de Berg, W.J., Bamber, J.L., Box, J.E., Bales, R.C., 2009. Higher surface mass balance of the Greenland ice sheet revealed by high-resolution climate modeling. Geophys. Res. Lett. 36, L12501. http://dx.doi.org/10.1029/2009GL038110.

Farrell, W.E., Clark, J.A., 1976. On Postglacial Sea Level. Geophys J Roy Agstr S 46 (3), 647–667.

Grinsted, A., Jevrejeva, S., Riva, R.E.M., Dahl-Jensen, D., 2015. Sea level rise projections for northern Europe under RCP8.5. Clim. Res. 64, 15–23. http://dx.doi.org/10.3354/cr01309.

Hallegatte, S., Green, C., Nicholls, R.J., Corfee-Morlot, J., 2013. Future flood losses in major coastal cities. Nat. Clim. Chang. 3, 802–806. http://dx.doi.org/10.1038/NCLIMATE1979.

Jevrejeva, S., Grinsted, A., Moore, J.C., 2014. Upper limit for sea level projections by 2100. Environ. Res. Lett. 9. http://dx.doi.org/10.1088/1748-9326/9/10/104008.

Kaneko, S., Toyota, T., 2011. Long-term urbanization and land subsidence in asian megacities: an indicators system approach. In: Taniguchi, M. (Ed.), Groundwater and Subsurface Environments: Human Impacts in Asian Coastal Cities. Springer, Japan, pp. 249–270.

Kopp, R.E., Horton, R.M., Little, C.M., Mitrovica, J.X., Oppenheimer, M., Rasmussen, D.J., Strauss, B.H., Tebaldi, C., 2014. Probabilistic 21st and 22nd century sea-level projections at a global network of tide-gauge sites. Earth's Future 2, 383–406. http://dx.doi.org/10.1002/2014EF000239.

Lagarias, J.C., Reeds, J.A., Wright, M.H., Wright, P.E., 1998. Convergence properties of the Nelder-mead simplex method in low dimensions. SIAM J Optimiz 9 (1), 112–147.

Lambeck, K., Yokoyama, Y., Purcell, A., 2002. Into and out of the last glacial Maximum Sea level change during oxygen isotope stages 3-2. Quat. Sci. Rev. 21, 343–360.

Lambeck, K., Purcell, A., Johnston, P., Nakada, M., Yokoyama, Y., 2003. Water-load definition in the glacio-hydro-isostatic sea-level equation. Quat. Sci. Rev. 22, 309–318.

Landerer, F.W., Jungclaus, J.H., Marotzke, J., 2007. Regional dynamic and steric sea level change in response to the IPCC-A1B scenario. J. Phys. Oceanogr. http://dx.doi.org/10.1007/s00382-013-1939-x.

Landerer, F.W., Gleckler, P.J., Lee, T., 2014. Evaluation of CMIP5 dynamic sea surface height multi-model simulations against satellite observations. Clim. Dyn. (5), 1271–1283 http://dx.doi.org/10.1007/s00382-013-1939-x.

Levermann, A., Winkelmann, R., Nowicki, S., Fastook, J.L., Frieler, K., Greve, R., Hellmer, H.H., Martin, M.A., Meinshausen, M., Mengel, M., Payne, A.J., Pollard, D., Sato, T., Timmermann, R., Wang, W.L., Bindschadler, R.A., 2014. Projecting Antarctic ice discharge using response functions from SeaRISE ice-sheet models. Earth Syst. Dynam. 5, 271–293. http://dx.doi.org/10.5194/esd-5-271-2014.

Little, C.M., Oppenheimer, M., Urban, N.M., 2013. Upper bounds on twenty-first-century Antarctic ice loss assessed using a probabilistic framework. Nat. Clim. Chang. 3, 654–659. http://dx.doi.org/10.1038/NCLIMATE1845.

Little, C.M., Horton, R.M., Kopp, R.E., Oppenheimer, M., Yip, S., 2015. Uncertainty in twenty-first-century CMIP5 sea level projections. J. Clim. 28, 838–852. http://dx.doi.org/10.1175/JCLI-D-14-00453.1.

Lucarini, V., Ragone, F., 2011. Energetics of climate models: net energy balance and meridional enthalpy transport. Rev. Geophys. 49, RG1001. http://dx.doi.org/10.1029/2009RG000323.

Marzeion, B., Jarosch, A.H., Hofer, M., 2012. Past and future sea-level change from the surface mass balance of glaciers. Cryosphere 6, 1295–1322. http://dx.doi.org/10.5194/tc-6-1295-2012.

Massey, F.J., 1951. The Kolmogorov-Smirnov test for goodness of fit. J. Am. Stat. Assoc. 46 (253), 68–78.

Miller, K.G., Kopp, R.E., Horton, B.P., Browning, J.V., Kemp, A.C., 2013. A geological perspective on sea-level rise and impacts along the U.S. mid-Atlantic coast. Earth's Future 1, 3–18. http://dx.doi.org/10.1002/2013EF000135.

Milne, G.A., Mitrovica, J.X., 1998a. Postglacial Sea-level change on a rotating earth. Geophys. J. Int. 133, 1–19.
Milne, G.A., Mitrovica, J.X., 1998b. The influence of time-dependant ocean-continent geometry on predictions of post-glacial sea level change in Australia and New Zealand. Geophys. Res. Lett. 25 (6), 793–796.
Mitrovica, J.X., Milne, G.A., 2003. On post-glacial sea level: I. general theory. Geophys. J. Int. 154 (2), 253–267.
Mitrovica, J.X., Peltier, W.R., 1991. On postglacial geoid subsidence over the equatorial oceans. J. Geophys. Res. 96 (B12), 20,053–20,071.
Mitrovica, J.X., Gomez, N., Clark, P.U., 2009. The sea-level fingerprint of West Antarctic collapse. Science 323 (5915), 753. http://dx.doi.org/10.1126/science.1166510.
Mitrovica, J.X., Gomez, N., Morrow, E., Hay, C., Latychev, K., Tamisiea, M.E., 2011. On the robustness of predictions of sea level fingerprints. Geophys. J. Int. 187 (2), 729–742. http://dx.doi.org/10.1111/j.1365-246X.2011.05090.x.
Moon, T., Joughin, I., Smith, B., Howat, I., 2012. 21st-century evolution of Greenland outlet glacier velocities. Science 336, 576–578. http://dx.doi.org/10.1126/science.1219985.
Moss, R.H., Edmonds, J.A., Hibbard, K.A., Manning, M.R., Rose, S.K., van Vuuren, D.P., Carter, T.R., Emori, S., Kainuma, M., Kram, T., Meehl, G.A., Mitchell, J.F.B., Nakićenović, N., Riahi, K., Smith, S.J., Stouffer, R.J., Thomson, A.M., Weyant, J.P., Wilibanks, T.J., 2010. The next generation of scenarios for climate change research and assessment. Nature 463, 747–756. http://dx.doi.org/10.1038/nature08823.
Nakićenović, N., Swart, R. (Eds.), 2000. Special Report on Emissions Scenarios. Cambridge University Press (559 pp).
Oppenheimer, M., Little, C.M., Cooke, R.M., 2016. Expert judgement and uncertainty quantification for climate change. Nat. Clim. Chang. 6, 445–451. http://dx.doi.org/10.1038/NCLIMATE2959.
Peltier, W.R., 2004. Global glacial Isostacy and the surface of the ice-age earth: the ICE-5G (VM2) model and GRACE. Annu. Rev. Earth Planet. Sci. 32, 111–149. http://dx.doi.org/10.1146/annurev.earth.32.082503.144359.
Peltier, W.R., Argus, D.F., Drummond, R., 2015. Space geodesy constrains ice age terminal deglaciation: the global ICE-6G C (VM5a) model. J. Geophys. Res. Solid Earth 119. http://dx.doi.org/10.1002/2014JB011176.
Perrette, M., Landerer, F., Riva, R., Frieler, K., Meinshausen, M., 2013. A scaling approach to project sea level rise and its uncertainties. Earth Syst. Dynam. 4, 11–29. http://dx.doi.org/10.5194/esd-4-11-2013.
Pfeffer, W.T., Harper, J.T., O'Neel, S., 2008. Kinematic constraints on glacier contributions to 21st-century sea-level rise. Science 321, 1340–1343. http://dx.doi.org/10.1126/science.1159099.
Pollard, D., Deconto, R.M., Alley, R.B., 2015. Potential Antarctic Ice Sheet retreat driven by hydrofracturing and ice cliff failure. Earth Planet. Sci. Lett. 412, 112–121. http://dx.doi.org/10.1016/j.epsl.2014.12.035.
Richter, K., Riva, R.E.M., Drange, H., 2013. Impact of self-attraction and loading effects induced by shelf mass loading on projected regional sea level rise. Geophys. Res. Lett. 40, 1144–1148. http://dx.doi.org/10.1002/grl.50265.
Rignot, E., Koppes, M., Velicogna, I., 2010. Rapid submarine melting of the calving faces of West Greenland glaciers. Nat. Geosci. 3, 187–191. http://dx.doi.org/10.1038/NGEO765.
Rignot, E., Fenty, I., Xu, Y., Cai, C., Velicogna, I., Cofaigh, C.Ó., Dowdeswell, J.A., Weinrebe, W., Catania, G., Duncan, D., 2016. Bathymetry data reveal glaciers vulnerable to ice-ocean interaction in Uummannaq and Vaigat glacial fjords, west Greenland. Geophys. Res. Lett. 43. http://dx.doi.org/10.1002/2016GL067832.
Ritz, C., Edwards, T.L., Durand, G., Payne, A.J., Peyaud, V., Hindmarsk, R.C.A., 2015. Potential sea-level rise from Antarctic ice-sheet instability constrained by observations. Nature 528, 115–118. http://dx.doi.org/10.1038/nature16147.
Rosner, B., 1983. Percentage points for a generalized ESD many-outlier procedure. Technometrics 25, 165–172.
Rowley, R.J., Kostelnick, J.C., Braaten, D., Li, X., Meisel, J., 2007. Risk of rising sea level to population and land area. EOS Trans. Am. Geophys. Union 88 (9), 105–116. http://dx.doi.org/10.1029/2007EO090001.
Sen Gupta, A., Muir, L.C., Brown, J.N., Phipps, S.J., Durack, P.J., Monselesan, D., Wijffels, S.E., 2012. Climate drift in the CMIP3 models. J. Clim. 25, 4621–4640. http://dx.doi.org/10.1175/JCLI-D-11-00312.1.
Sen Gupta, A., Jourdain, N.C., Brown, J.N., Monselesan, D., 2013. Climate drift in the CMIP5 models. J. Clim. 26, 8597–8615. http://dx.doi.org/10.1175/JCLI-D-12-00521.1.
Slangen, A.B.A., Carson, M., Katsman, C.A., van de Wal, R.S.W., Köhl, A., Vermeersen, L.L.A., Stammer, D., 2014a. Projecting twenty-first century regional sea-level changes. Clim. Chang. http://dx.doi.org/10.1007/s10584-014-1080-9.
Slangen, A.B.A., Church, J.A., Zhang, X., Monselesan, D., 2014b. Detection and attribution of global mean thermosteric sea level change. Geophys. Res. Lett. 41, 5951–5959. http://dx.doi.org/10.1002/2014GL061356.
Spada, G., Stocchi, P., 2007. SELEN: a Fortran 90 program for solving the "sea-level equation". Comput. Geosci. 33 (4), 538–562. http://dx.doi.org/10.1016/j.cageo.2006.08.006.
Spada, G., Bamber, J.L., Hurkmans, R.T.W.L., 2013. The gravitationally consistent sea-level fingerprint of future terrestrial ice loss. Geophys. Res. Lett. 40, 482–486. http://dx.doi.org/10.1029/2012GL053000.
Sriver, R.L., Urban, N.M., Olson, R., Keller, K., 2012. Toward a physically plausible upper bound of sea-level rise projections. Clim. Chang. 115 (3–4), 893–902. http://dx.doi.org/10.1007/s10584-012-0610-6.
Stammer, D., Hüttmann, S., 2008. Response of regional sea level to atmospheric pressure loading in a climate change scenario. J. Clim. 21, 2093–2101. http://dx.doi.org/10.1175/2007JCLI1803.1.
Tadikamalla, P.R., 1980. A look at the Burr and related distributions. Int. Stat. Rev. 48 (3), 337–344.
Tamisiea, M.E., Mitrovica, J.X., 2011. The moving boundaries of sea level change. Oceanography 24 (2), 24–39. http://dx.doi.org/10.5670/oceanog.2011.25.
Tamisiea, M.E., Hill, E.M., Ponte, R.M., Davis, J.L., Velicogna, I., Vinogradova, N.T., 2010. Impact of self-attraction and loading on the annual cycle in sea level. J. Geophys. Res. 115, C07004. http://dx.doi.org/10.1029/2009JC005687.1.
Taylor, K.E., Stouffer, R.J., Meehl, G.E., 2012. An overview of CMIP5 and the experiment design. B Am Meteorol Soc 93, 485–498. http://dx.doi.org/10.1175/BAMS-D-11-00094.1.
van der Wal, W., Barnhoorn, A., Stocchi, P., Gradmann, S., Wu, P., Drury, M., Vermeersen, B., 2013. Glacial isostatic adjustment model with composite 3-D earth rheology for Fennoscandia. Geophys. J. Int. 194 (1), 61–77. http://dx.doi.org/10.1093/gji/ggt099.
Wada, Y., van Beek, L.P.H., Weiland, F.C.S., Chao, B.F., Wu, Y.-H., Bierkens, M.F.P., 2012. Past and future contribution of global groundwater depletion to sea-level rise. Geophys. Res. Lett. 39, L09402. http://dx.doi.org/10.1029/2012GL051230.
Yin, J., 2012. Century to multi-century sea level rise projections from CMIP5 models. Geophys. Res. Lett. 39, L17709. http://dx.doi.org/10.1029/2012GL052947.
Yin, J., Griffies, S.M., Stouffer, R.J., 2010. Spatial variability of sea level rise in twenty-first century projections. J. Clim. 23, 4585–4607. http://dx.doi.org/10.1175/2010JCLI3533.1.